12-2017

Anti-Icing Properties of Femtosecond Laser Surface Processed Material

Ryan James Bell
University of Nebraska-Lincoln

ANTI-ICING PROPERTIES

OF FEMTOSECOND LASER SURFACE PROCESSED MATERIAL

By

Ryan James Bell

A THESIS

Presented to the Faculty of

The Graduate College at the University of Nebraska

In Partial Fulfillment of Requirements

For the Degree of Master of Science

Major: Electrical Engineering

Under the Supervision of Professor Dennis Alexander

Lincoln, Nebraska

December, 2017

ANTI-ICING PROPERTIES

OF FEMTOSECOND LASER SURFACE PROCESSED MATERIAL

Ryan James Bell, M.S.

University of Nebraska, 2017

Advisor: Dennis Alexander

In this thesis, the use of femtosecond laser surface processing (FLSP) to enhance the anti-icing properties of a commonly used aircraft alloy, Al 7075-O Clad is described. By changing the surface morphology through FLSP and the surface chemistry through siloxane vapor deposition, the wettability of Al 7075-O Clad was altered.

Condensation and the subsequent freezing of condensates on FLSP Al 7075-O Clad was studied. Both structure height and surface wettability were shown to play a role in the delay of freezing. Freezing occurred on the FLSP superhydrophilic surface faster than on the unprocessed Al 7075-O Clad surface, however, freezing was delayed for all superhydrophobic FLSP surfaces. Tall structure height FLSP functionalized surfaces delayed freezing time longer than short structure height FLSP functionalized surfaces although all were superhydrophobic. It was shown that FLSP functionalized surfaces were able to delay freezing by up to 530 seconds compared to unprocessed Al 7075-O Clad. Self-propelled condensate jumping on FLSP surfaces occurs during the condensing process. The self-propelled jumping phenomena provides a means to promote anti-icing of materials, especially where jumping drops can be swept away in flow conditions

The dynamics of supercooled water droplet impact onto FLSP and unprocessed surfaces was also studied. Imaging of supercooled water droplet interaction dynamics on a solid Al 7075-O Clad cold substrate for a droplet diameter below 160 µm is shown for

the first time. Results indicate that microscale supercooled water droplets at low velocities will stick and freeze to unprocessed Al 7075-O Clad surfaces, while FLSP surfaces will repel droplets under similar conditions. A method for estimating the cooling of small falling water droplets in an environment of about -16 °C is described. This method gives insights for determining the temperature of supercooled droplets for the range of droplet diameters used in the experimental studies included in this paper. In addition, a way to estimate the nucleation site of a supercooled droplet by extrapolation of dendrite front velocity is provided.

Acknowledgements

I cannot say thank you enough to all who have helped me during both my undergraduate and graduate career. The list of those who have lent both their hands and insight along the way is too numerous to include, however, there are a few people who I would especially like to thank.

I would like to thank all who have made the Center for Electro-Optics and Functionalized Surfaces possible. Working in this group has been an absolute dream come true. Special thanks to my advisor, Dr. Dennis Alexander, for all your insight on not only research, but also life. I appreciate you always pushing me to excel in everything I do.

Thanks to Dr. Craig Zuhlke for his ability to always have the correct solution to any problem. Craig has had a massive impact on molding my way of thinking. I hold Craig in an extremely high regard, and want to make sure he knows how much he has positively impacted me as both a scientist and a person.

Also thanks to Dr. George Gogos and Dr. Ned Ianno for not only serving on my examination committee, but also for being constant sources of both great conversation and strong scientific insight.

I would also like to thank Dr. John Woollam I will forever be grateful for not only the financial support, but also for the opportunity to call you a mentor.

Thanks to my labmates; Alfred Tsubaki, Conner Thomas, Chongji Huang, Nick Roth, and Aaron Ediger. I am extremely lucky to have had the opportunity to call you my colleagues and friends. I truly could not have asked for a better group of people to work with. Thanks to my friends outside of research. Unfortunately, this is the end of my sweet laser snapchats. Thanks for still being my friends even after my "femto something manufacturing" talks became too much.

Finally, I would like to thank my family. A special thanks to my parents Doug and Laura Bell and my sister and brother-in-law Dana and Cody Raml. You have been a wonderful support group. Thanks for all the love and support throughout the years.

You all have played large roles in my growth as both a scholar and person. Other than a few more Husker victories, I truly could not have asked for anything more during my time at the University of Nebraska. For that, I extend a sincere thank you.

Table of Contents

List of Tables

List of Figures

Chapter 1

Dynamics of ice formation

As water is cooled below its freezing point it enters a thermodynamically metastable liquid state commonly known as supercooled. Supercooled water will freeze if an event occurs to trigger ice nucleation. Although the fundamental mechanism of nucleation in the freezing of water is not currently understood [1, 2], nucleation can be predicted using classical nucleation theory [3, 4]. Following the classical nucleation theory, the formation of an ice nucleus in supercooled water requires excess Gibbs free energy to overcome the nucleation barrier [5]. The nucleation barrier is a function of surface wettability [6], thus, the heterogeneous critical energy barrier of a superhydrophobic surface approaches the homogeneous critical energy barrier [7]. Nucleation of ice within the supercooled droplet can be triggered through a variety of means including: impurities in the water [8], mechanical shock [3], thermal fluctuation [9], or contact with a cooled surface [2]. By limiting perturbations that can trigger ice nucleation, Goy et al. [10] have shown the ability to cool bulk water to temperatures as low as -42.55 °C in a low pressure environment.

Nucleation is expected to initiate at the solid-liquid interface as the heterogeneous critical activation energy is lower [6], although nucleation has also been shown to initiate at the liquid-vapor interface under a sufficient shearing gas flow [11]. Once nucleation has initiated, supercooled freezing of the volume occurs. Supercooled droplet freezing occurs in two phases. During the first phase, or recalescence phase, which occurs on the order of milliseconds, the temperature of the droplet is rapidly increased to thermodynamic equilibrium. It is a kinetically controlled process in which ice dendrites, originating from the nucleation site, propagate throughout the volume of the droplet [12]. The velocity and density of the dendritic front is largely dependent on the level of initial supercooling of the droplet [13]. The second phase of supercooled freezing, which occurs on the order of seconds, occurs at thermodynamic equilibrium. During this stage the

remaining liquid in the droplet freezes. In the case of sessile droplets, the freezing front originates at the substrate and propagates in the opposite direction of the heat flux [13]. The freezing front becomes curved due to boundary conditions at the triple phase contact line (TCL) [14, 15]. The curvature of the freezing front is responsible for the cusp that develops in frozen sessile droplets [16].

The rapid heating that occurs during recalescence causes a rapid evaporative effect during which a condensation halo develops [11]. If allowed to freeze this condensation halo can trigger nucleation in surrounding supercooled droplets that have not begun the freezing process [17–19]. Thus, the adhesion and freezing of any one droplet will subsequently lead to larger scale ice accumulation in sustained icing conditions such as droplet impacts during freezing rain.

Chapter 2

Femtosecond laser surface processing of Al 7075-O Clad

FLSP is unique surface functionalization technology in the fact that the surfaces produced are composed of microscale structures covered with nanoscale particles produced in a single processing step [20]. FLSP surfaces can be made superhydrophobic through a variety of methods used to lower the surface energy of the micro and nanoscale textured surfaces, including vapor deposition of low surface energy molecules or adsorption of adventitious carbon from a hydrocarbon rich atmosphere.

2.1 Various structures created on Al 7075-O Clad

FLSP is commonly performed by rastering the Gaussian beam profile across a surface in a raster pattern. The throughput when rastering is typically higher than with a TH beam. A typical FLSP processing setup is shown in Figure 2.1.
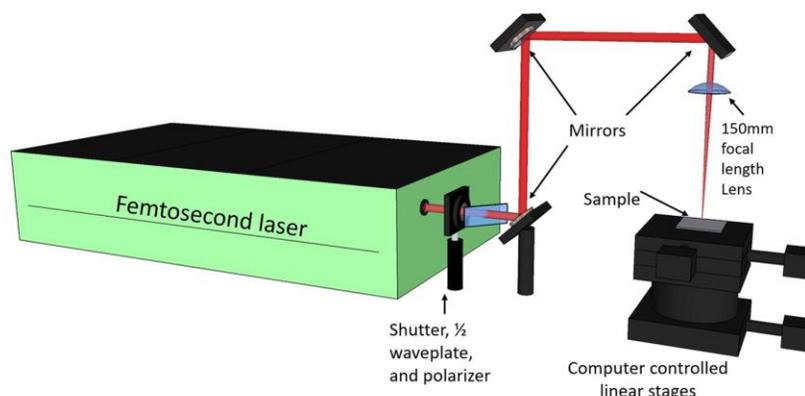
Figure 2.1: Schematic of the femtosecond laser surface processing setup used in this work.

When rastering with a Gaussian beam profile, fluence becomes a function of the beam diameter at the surface and the average power. This method is shown in more detail by Liu [21]. When using the Gaussian beam in the raster, calculating the fluence and the

shot number incident to the surface becomes more complex. The shot number becomes a function of the total number of overlapping pulses at each unit area. In common laboratory practice, the fluence at the processed surface is controlled through a $\lambda/4$-waveplate and polarizer combination, a focusing optic, and a linear stage while the shot number is controlled by beam diameter, the pitch of the raster, and translational speed of the translational stages.

Just as Zuhlke et al. [22] have shown on other materials, the laser parameters used during FLSP of Al 7075-O Clad has an impact on the size and structures formed. Structures formed by FLSP on Al 7075-O Clad are shown at 12 combinations of 4 fluences and 3 pulse count are shown in Figure 2.2. The structures were imaged using an SEM and laser scanning confocal microscope (LSCM) (Keyence VK-X200K).
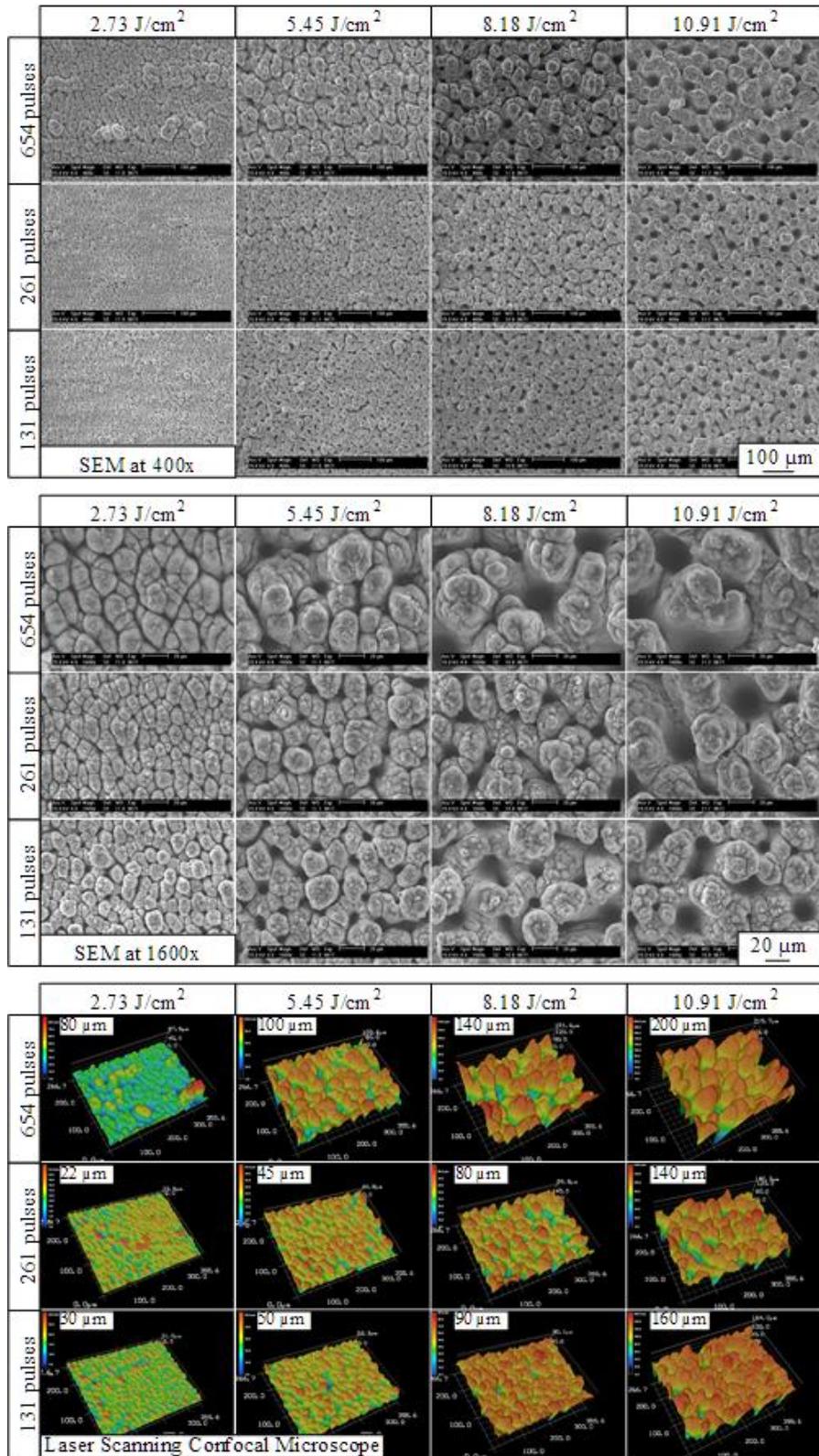
Figure 2.2: Al 7075-O Clad Processed at 12 different combinations of fluence and shot number. Images shown are: SEM at 400x magnification (top), SEM images at 1600x magnification (center), and with 3D LSCM.

By analyzing the LSCM images with Keyence Analyze software, the change in microstructure of the Al 7075-O Clad surface change be quantified. These arbitrarily chosen fluence and pulse number were shown to produce surfaces structures that varied drastically. For the range of fluence and pulse count FLSP produced surfaces with a microscale roughness spanning from 2.3 to 29.6 µm, an average maximum structure height from 21.9 to 184.9 µm, and a surface area to geometric area ratio from 1.7 to 3.9.

Note: The average roughness, average structure peak to valley height, and surface area to geometric area ratio for all combinations of fluence and pulse count on FLSP Al 7075-O Clad is shown in the appendix beginning on page 44.

Chapter 3

Condensation and subsequent freezing delay as a result of using FLSP surfaces

There are many applications where metallic anti-icing surfaces would be desirable. Typical applications include power line cables, aircraft, wind turbines, and cold weather marine applications. Various anti-icing studies have been reported in previous publications [23–26]. Surface wettability, which can be controlled by micro/nanoscale features along with surface chemistry, is an important parameter for controlling ice buildup. Superhydrophobic and hydrophobic surfaces have been shown to delay freezing on various substrates [23–25, 27–31]. In work by Van Dyke et al. [31], the relative humidity of the atmosphere was shown to be an important factor in icing due to condensation.

Femtosecond laser surface processing (FLSP) has been previously shown to produce different self-organized micro/nanoscale surfaces on metals [22]. Structures produced through FLSP can be controlled by varying the laser fluence and pulse count. FLSP surfaces can be made superhydrophobic by vapor deposition. In this chapter, the delay of condensation and subsequent freezing on superhydrophobic and superhydrophilic FLSP functionalized and unprocessed Al 7075-O Clad surfaces is investigated. Superhydrophobic FLSP functionalized tall mound surface delayed the time required for freezing of condensation the longest. This is the first time that the impact of FLSP structures on the time required for freezing of condensation to occur.

Condensate on superhydrophobic surfaces has been shown to spontaneously jump upon coalescence [32]. Self-propelled condensate jumping exhibits a self-cleaning effect which has been shown to delay condensation and subsequent freezing time [33]. In this paper, self-propelled jumping condensate on FLSP functionalized surfaces is shown for the first time.

3.1   FLSP surfaces used for study of condensation and subsequent freezing delay

Quasiperiodic microstructures covered with nanoparticles, were produced through FLSP on various 40 by 40 by 1 mm Al 7075-O Clad aircraft aluminum alloy samples. The laser used in this work was a Coherent, Astrella laser system, which produces 35 fs, 800 nm pulses at a 1 kHz repetition rate, with a maximum pulse energy of 6 mJ. The size and shape of the FLSP micron scale features were modified by controlling the laser fluence and the number of laser pulses incident on the sample using a technique described by Zuhlke et al. [20, 22].

By varying the laser parameters, two different mound structures were created on Al 7075-O Clad. For tall mound surfaces, the laser fluence value was 6.03 J/cm2 and the laser spot radius was 200 µm. Each region was irradiated with 341 pulses. For the short mound surfaces, the laser fluence value was 2.80 J/cm2 and the laser spot radius was 282 µm. Each region was irradiated with 506 pulses. LSCM 3D view and SEM images of the unprocessed Al 7075-O Clad, and two structure subsets, SMS and TMS, are shown in Figure 3.1.
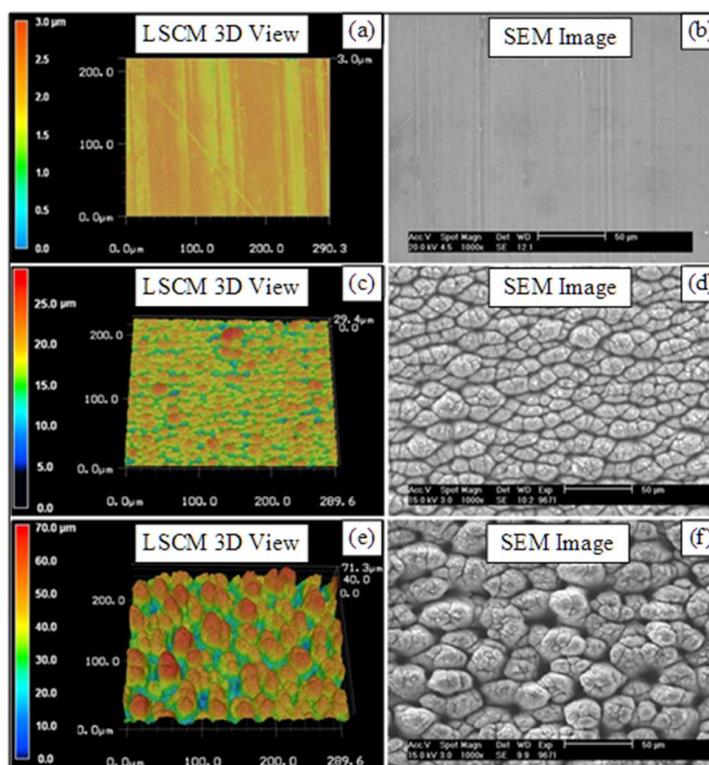
Figure 3.1: (a) LSCM 3D view of unprocessed Al 7075-O Clad, (b) SEM image of unprocessed Al 7075-O Clad, (c) LSCM 3D view of short mound surface, (d) SEM image of short mound surface, (e) LSCM 3D view of tall mound surface, (f) SEM image of tall mound surface.

The intrinsically superhydrophilic FLSP Al 7075-O Clad surfaces were made superhydrophobic (functionalized) through vapor deposition of VMQ O-rings (McMaster-Carr 9396k105). The FLSP samples and the O-rings were placed on a Thermolyne Cimarec 2 heater and covered with a glass filter funnel. The samples were placed radially around the O-rings. The FLSP surfaces were face up. The air temperature inside the funnel was kept at 182.1 °C, measured by a thermocouple suspended inside the funnel. The heater plate temperature was 263.4 °C, measured with a thermocouple rested on top of the heater plate. The vapor deposition period was 2 hours. For the first 20 minutes, the nozzle of the funnel was left open. After 20 minutes, aluminum foil was used to seal the nozzle. One tall mound surface sample was kept superhydrophilic (referred to as superhydrophilic). All other FLSP samples were made superhydrophobic through vapor deposition of siloxanes (referred to as SMS1, SMS2, TMS1, and TMS2).

The intrinsic contact angle of all samples was measured using a Ramé-hart Goniometer/Tensiometer Model 790 with DROPimage Advanced software. The water droplet size used for the contact angle measurements was 5 µL.

3.2 Condensation and subsequent delay of freezing

A Peltier cooler system was constructed with the following elements: a 2 Stage Peltier Module (Custom Thermoelectric 25412-5L31-07CQQ); a copper water block (Custom Thermoelectric WBA-1.62-0.55-CU-01); and a flat aluminum plate (Custom Thermoelectric CPT-2.25-1.62-0.25-AL). Excess heat from the Peltier cooler was dissipated through a copper cooling block supplied with chilled water at 5 °C supplied by a LYTRON circulating chiller (RC006G03BB1C002). The temperature of the flat aluminum plate was controlled with the following elements: a Kapton insulated K-type thermocouple (OMEGA 5TC-KK-K-20-72); a solid state relay (OMEGA SSRDC100VDC12); a PID Controller (OMEGA CNI-16D44); and a voltage supply (KEPCO JQE 25-10M). The thermocouple was secured and thermally bonded (Omega OT-20-1/2) in the compression mounting of the flat aluminum plate. Samples were placed on the flat aluminum plate. Dry nitrogen gas at a velocity of approximately 20 m/s was flowed over the samples to prevent condensation from occurring before the start of data collection. The voltage and current to the Peltier cooler were kept constant at 8 V and 3.85 A, respectively. The PID controller was set to -15 °C. The cycle time for the relay and PID controller was 1 second. The assembled temperature controlled Peltier cooler system is shown in Figure 3.2.
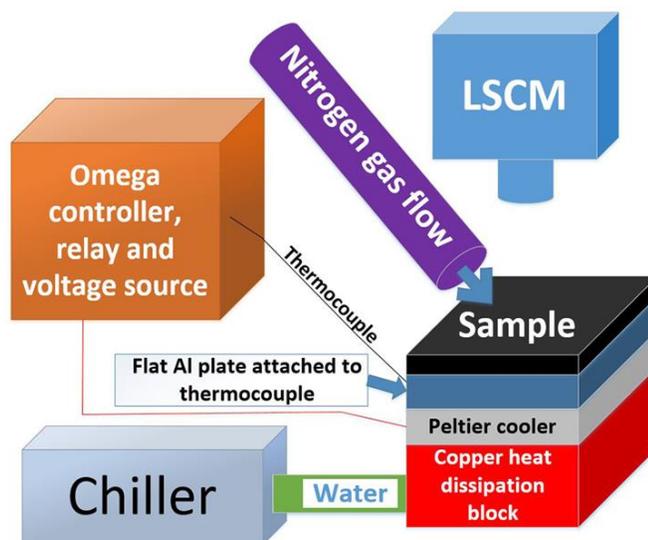
Figure 3.2: Diagram of thermoelectric cooler system.

With the nitrogen gas flow on and the Peltier on, the samples cooled from room temperature at 22 °C to -2.3 ± 0.2 °C (± as standard deviation). The nitrogen flow was stopped when data recording was initiated. The temperature of the samples further decreased from -2.3 °C to -15 °C, where it was kept constant by the PID controller switching the relay on and off. The relative humidity in the room was 25%. Humidity and room temperature were measured using a dual humidity and temperature meter (McMaster-Carr 39175K21). The Peltier cooler system was mounted on the Keyence Laser Scanning Confocal Microscope (LSCM) VK-X200K with the view centered on the samples. The LSCM optical microscope was used to monitor and record videos of the condensation and subsequent freezing on the samples. The LSCM was used to measure average structure height (Rz). The time required for condensate freezing is defined as when condensates from the atmosphere have frozen (solidified) over the entire surface being monitored by the optical view of the LSCM.

After removing the nitrogen flow from the samples, each sample followed a similar cooling rate to -15 °C as shown in Figure 3.3. It should be noted that the temperature of the superhydrophilic surface dropped faster than that of the other samples. The increased rate of temperature drop is contributed to the film condensation on the superhydrophilic surface which acts to insulate the surface from the atmosphere, while condensation on the other surfaces occurs in a dropwise manner.
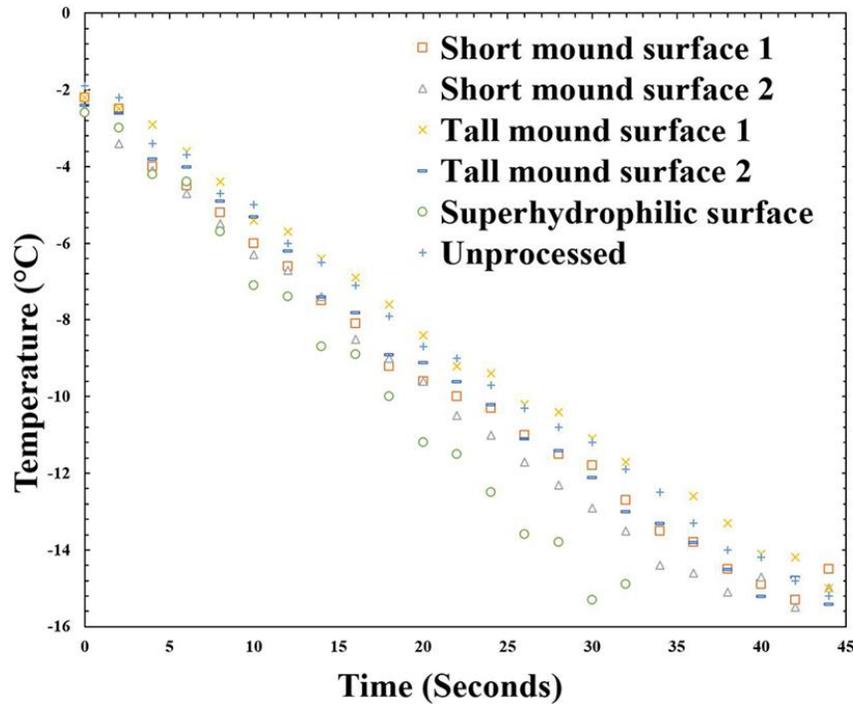
Figure 3.3: Initial sample cooling from -2.3 °C to -15 °C

    The average structure height, contact angle (CA) before and after experiment, and time for freezing of each sample are shown in Table 3.1. The time required to cool the samples to -15 °C is included in the entire surface freezing time.

Table 3.1: Sample surface characteristics, contact angle (CA) before and after the experiment, and condensation and subsequent freezing.

	Average Height R_z (µm)	CA Before Experiment (°)	CA After Experiment (°)	Entire Surface Freezing Time (s)
Unprocessed Al 7075-O Clad	1.2 ± 0.6	53 ± 9	77 ± 2	188
Superhydrophilic surface	55.3 ± 4.4	0	0	41
SMS1	21.2 ± 5.2	168 ± 2	168 ± 4	545
SMS2	16.9 ± 3.0	170 ± 4	168 ± 2	567
Average data of SMS	18.9 ± 4.8	169 ± 2	168 ± 3	556
TMS1	56.4 ± 7.8	168 ± 3	167 ± 2	696
TMS2	47.8 ± 4.3	169 ± 3	166 ± 1	718
Average data of TMS	53.3 ± 7.6	168 ± 3	167 ± 2	707

    The superhydrophilic sample froze faster (41 seconds) than the unprocessed sample (188 seconds). All superhydrophobic surfaces delayed freezing for at least 357 seconds after the unprocessed froze. It should be noted that the sample with a higher CA for each structure subset delayed freezing longer than their respective counterpart.

Surface chemistry plays an important role in the delay of condensate freezing on FLSP structures of similar height. For equivalent sized droplets on superhydrophobic surfaces, the contact area for heat conduction is inversely proportional to the contact angle of the surface. The impact of CA has been previously shown to delay freezing of condensation on other substrates [34].

TMS1 and TMS2 both delayed the onset of freezing longer than both SMS1 and SMS2. Thus, the structure morphology is important in delaying the freezing condensation. Both structure morphology and surface chemistry were important properties in delaying the onset of condensate freezing.

Still frame images (captured during LSCM optical view) of the progression of condensation and subsequent freezing on all samples subsets are shown in Figure 3.4. Note that as the condensates freeze [(c), (f), (i), and (l)] the transparency and shape of the condensates are altered. The frozen condensates on SMS are more opaque than those on the TMS indicating that prior to freezing, condensates on SMS exist at a higher supercooling than on TMS [13, 18]. The transparency change is a result of rapid kinetic freezing of the condensates [19].

14
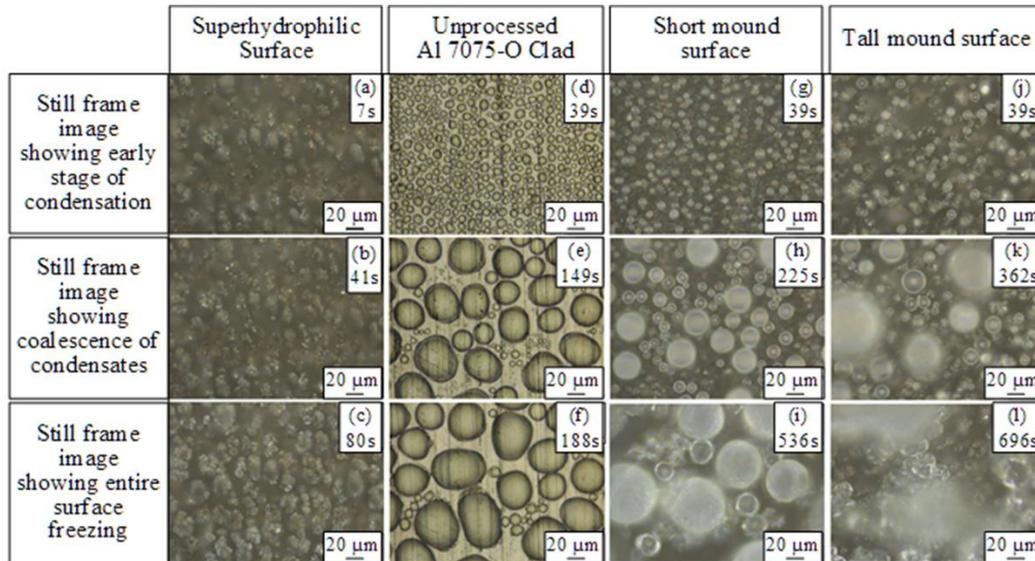
Figure 3.4: Condensation and subsequent freezing progression images of superhydrophilic FLSP functionalized surface shown in [(a), (b), and (c)]. Progression images of unprocessed Al 7075-O Clad surface shown in [(d), (e), and (f)]. Progression images of SMS shown in [(g), (h), and (i)]. Progression images of TMS shown in [(j), (k), and (l)]. The videos of entire surface freezing for each sample are shown in video 1, video 2, video 3, and video 4. The description and explanation for video 1 - 4 is in the supplementary material.

As shown in Figure 3.4, water vapor condenses into droplets on the unprocessed surface (d), SMS (g) and TMS (j), and the condensate drops grow [(e), (h), and (k)], coalesce and eventually freeze [(f), (i), and (l)]. On the superhydrophilic sample, condensate droplets are not easily observed, however, the growth and eventual freezing of a film of ice on the surface was observed (c).

3.3 Self-propelled jumping condensates on FLSP surfaces

Self-propelled jumping condensates on FLSP functionalized Al 7075-O Clad surfaces was observed at 8000 fps and recorded using a Photron FASTCAM SA 1.1 HighSpeed camera, with a Nikon NIKKOR 105mm 1:2.8G ED micro lens and 100 mm extensions tubes for increased magnification. The camera was at an incident angle of approximately 45° to the samples. A Fiber-Lite high-intensity illuminator series 180 was used to illuminate the sample.

The samples' temperatures were dropped from room temperature at 18.5 °C and were maintained at -7 °C by the PID controller. The temperature of the samples was controlled with the Peltier cooler system with no nitrogen flow. The relative humidity of the room was 25%.

Condensates on TMS and SMS exhibit self-propelled jumping away from the FLSP surface. Although self-propelled condensate jumping has been shown on other superhydrophobic surfaces[33], it is the first time self-propelled jumping has been reported in the literature on FLSP surfaces. A still image sequence of self-propelled condensate jumping on TMS1 is shown in Figure 3.5
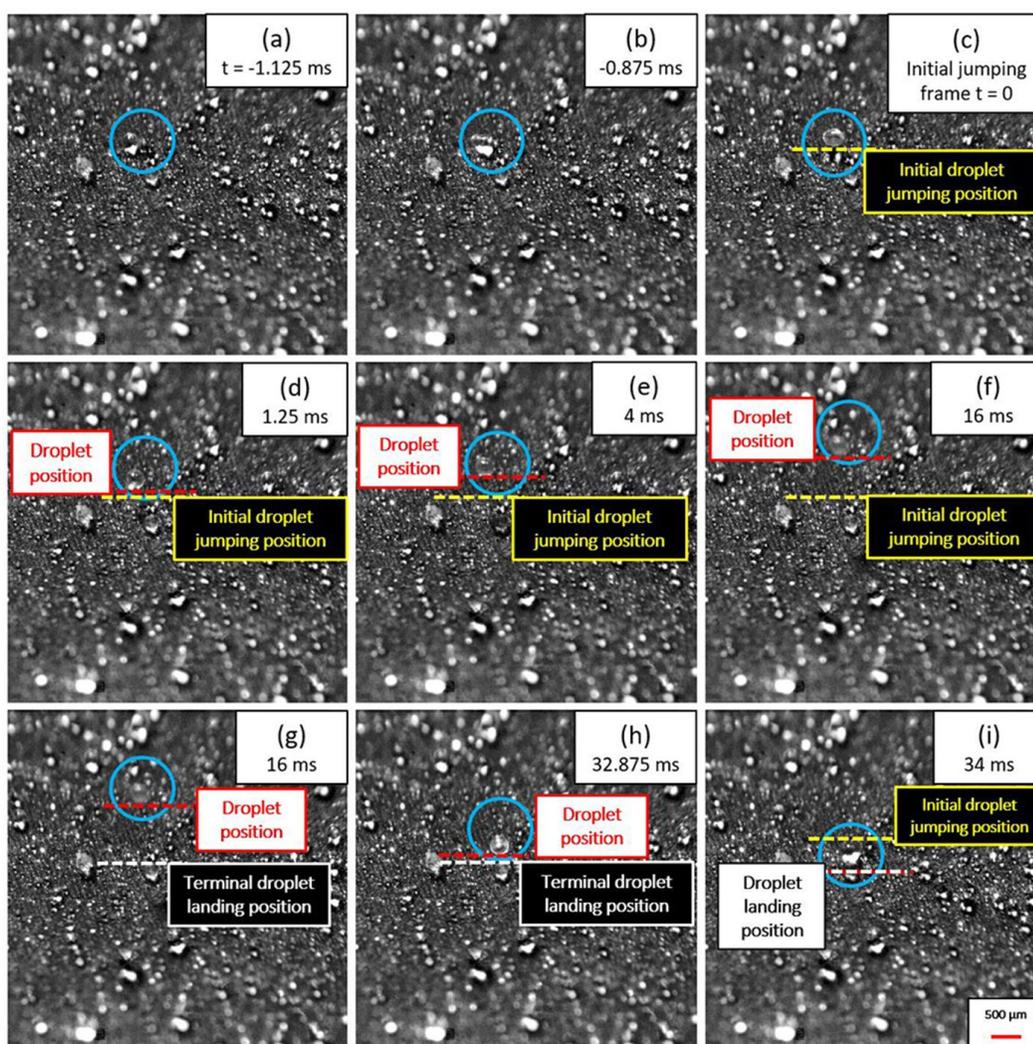
Figure 3.5: Still frame images of two condensate drops combining [(a), (b), and(c)], jumping off the surface [(d), (e), and (f)] and falling due to gravity [(g), (h), and (i)]. The video of this progression is shown in video 5.

Self-propelled condensate jumping is important for delaying the time required for freezing of condensation, as it acts to remove droplets which can initiate freezing on the surface. Self-propelled condensate jumping is strongly influenced by the wettability. Wisdom et al. [33] demonstrated a unique self-cleaning mechanism whereby the contaminated superhydrophobic surface is exposed to condensing water vapor, and the contaminants are autonomously removed by the self-propelled jumping motion of the resulting liquid condensate, which partially covers or fully encloses the contaminating particles. The higher the contact angle, the lower the energy required to detach a spherical particle from a flat interface [35].

3.4 Conclusion

In this work, different FLSP functionalized Al 7075-O Clad samples were processed with different surface structures. The freezing time of unprocessed Al 7075-O Clad was 188 second. The freezing time of superhydrophilic FLSP functionalized Al 7075-O Clad surface was 41 seconds. The freezing time of SMS1 and SMS2 was 556 ± 11 seconds. The freezing time of TMS1 and TMS2 was 707 ± 11 seconds. Self-propelled condensate jumping on FLSP structures is shown for the first time.

Chapter 4

FLSP as a means to prevent icing during supercooled liquid droplet impact

In the search for a truly icephobic surface, many studies have focused on the dynamics of droplet impact for various droplet diameters, droplet temperatures, and impact velocities on surfaces with varied surface structures and wetting properties [3, 27, 36–46]. The droplet diameters of previous icing studies are largely within the range specified in the Federal Airline Regulations Part 25 Appendix C (FAR25-C) [47], which defines the region of interest for the diameter of supercooled large drops as 50 µm to 2000 µm. Supercooled droplets with a diameter below 400 µm are in large part unstudied. To the best of our knowledge, the smallest diameter of supercooled droplet impact on a solid surface previously studied is 350 µm [43]. Quero et al. [48] present icing results using supercooled droplets as small as the droplets being reported in this study, however, that work was limited to droplet impact with thin films of water. The current study focuses on the lower end of the droplet diameter range specified in FAR25-C, extending the current limits of droplet diameter used in supercooled droplet impact onto solid substrates. This study utilizes femtosecond laser surface processing (FLSP) as a means to prevent the adhesion and eventual freezing of microscale supercooled droplets upon impact.

4.1 FLSP surfaces used for the study of ice formation during impact of supercooled liquid water droplets

Two Al 7075-O Clad samples were cut to 40 mm by 40 mm. Both samples were cleaned of any residual machining oils through 20 minute ultrasonic baths in acetone, methanol, and deionized water. The surface morphology of one Al 7075-O Clad sample was left unaltered. This sample will be referred to as the "unprocessed surface". The

surface morphology of the other sample was altered through FLSP. This sample will be referred to as the "FLSP surface". FLSP was performed using a Coherent Astrella Ultrafast Ti:Sapphire Amplifier, which was capable of producing 6 mJ, 35 fs pulses, centered at 800 nm with a repetition rate of 1 kHz. The Gaussian beam was focused to a spot radius of 282.00 µm yielding a peak laser fluence of 2.80 J/cm^2. When rastered using a pitch of 50 µm and translational speed of 80 mm/s, the combination of spot size, pitch and translational speed resulted in each area of the laser processed region being irradiated with 506 pulses of varying intensities (due to the Guassian spatial profile of the focused pulses). A laser scanning confocal microscope (LSCM) (Keyence VK-X200K) was used to determine the average structure height (R_z) of the unprocessed and FLSP surfaces.

The intrinsically superhydrophilic FLSP surface was made superhydrophobic through vapor deposition of siloxanes from VMQ O-rings (McMaster-Carr 9396k105). The FLSP surface was placed processed surface face-up on a Thermolyne Cimarec 2 heater. VMQ O-rings were placed surrounding the FLSP surface and covered with a glass funnel. The heater plate was kept at 263.4 °C, as measured by a thermocouple placed directly on the surface of the heater, for two hours. The temperature of the air inside the funnel was kept relatively constant at 182.1 °C, as measured by a thermocouple inside the funnel that was suspended approximately 2 cm from the heater surface. For the first 20 minutes of deposition, the opening of the funnel was left uncovered. After the first twenty minutes, the funnel opening was tightly covered with aluminum foil. After two hours, the heater plate was turned off and allowed to cool prior to removing the glass funnel.

The contact angle of the FLSP surface was measured using a Ramé-hart Goniometer/Tensiometer Model 790 with DROPimage Advanced software. The water droplet size used for the contact angle measurements was 5 µL. Wu et al. [49] have shown that tilting angle is more strongly correlated to droplet adhesion force than contact angle hysteresis. Thus, in the current study, tilting angle is used for characterizing droplet adhesion on the surfaces. Furthermore, a surface with a low contact angle hysteresis will also exhibit a low tilting angle.

After cleaning the samples, as described in the sample fabrication section, the contact angle of the unprocessed surface was $79.2 \pm 4.6°$. The droplet would not release even at an angle of $180°$. After VMQ vapor deposition, the contact angle of the FLSP surface was $168.4 \pm 1.1°$ with a tilting angle less than $1°$. Average R_z values for the unprocessed surface and FLSP surface, as measured using the LSCM, was determined to be 1.2 ± 0.6 µm and 21.2 ± 5.2 µm respectively. LSCM and SEM images of the unprocessed surface (a, b) and FLSP surface (c, d) are shown in Figure 4.1.
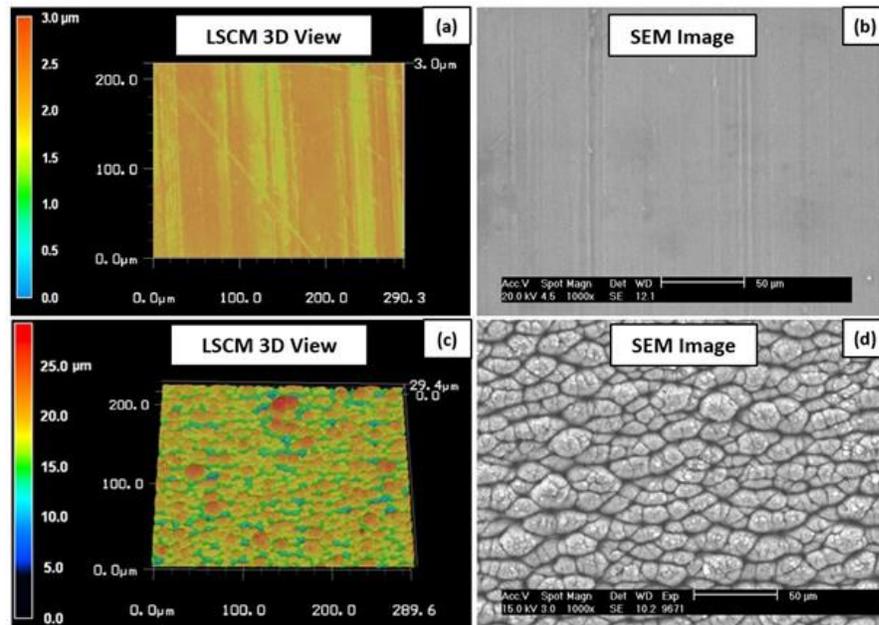
Figure 4.1: (a) LSCM 3D view of unprocessed Al 7075-O Clad, (b) SEM image of unprocessed Al 7075-O Clad, (c) LSCM 3D view of FLSP surface, (d) SEM image of FLSP surface.

4.2 Supercooled droplet impact study

Supercooled droplet impact studies were conducted in 800 cubic foot Russells walk-in thermal chamber at the Nebraska Center for Electronic Excellence (NCEE).

The water used has a nominal resistivity of 18.2 MΩ-cm (Barnstead Nanopure Life Science UV/UF D11931). Water Droplets were mono-dispersed from a Berglund-Liu aerosol generator (TSI Model 3941). A nominal droplet diameter of 100 µm was obtained by setting the aerosol generator frequency to 18.25 kHz and pump speed to 1.8E-3 cm/s with an orifice diameter of 50 µm. At these settings, the aerosol generator

dispersed droplets at an initial velocity of 4.867 m/s. The droplet generator and orifice were contained in an insulated box, and positioned approximately 65 cm above the sample surface. The temperature controlled box was held at 0 °C through a 170 watt heater (McMaster-Carr 1733K11) and a digital thermostat (Kegco TC-321). The droplets cooled as they fell the 65 cm to the sample surface, with a room temperature of -16 °C. The unprocessed surface and FLSP surface were mounted at 45° incident to the incoming direction of the free falling water droplets.

Individual droplet impact was recorded with a high-speed imaging system (Photron FASTCAM SA 1.1 with a Nikon AF-S VR Micro-NIKKOR 105mm 1:2.8G ED lens and 100mm extension tubes) at 15000 fps (66.7 µs between each frame). A microscope calibration slide was used as a length calibration source, so that the droplet size and velocity in the high-speed videos could be converted from pixels to microns. For all high-speed videos, a scale of 1 pixel to 10 microns was used. The samples were illuminated using fiber lights (Fiber-Lite high-intensity illuminator Series 180). The experimental setup for imaging the microscale supercooled liquid water droplets impacting FLSP and unprocessed Al 7075-O Clad surfaces is shown in Figure 4.2.
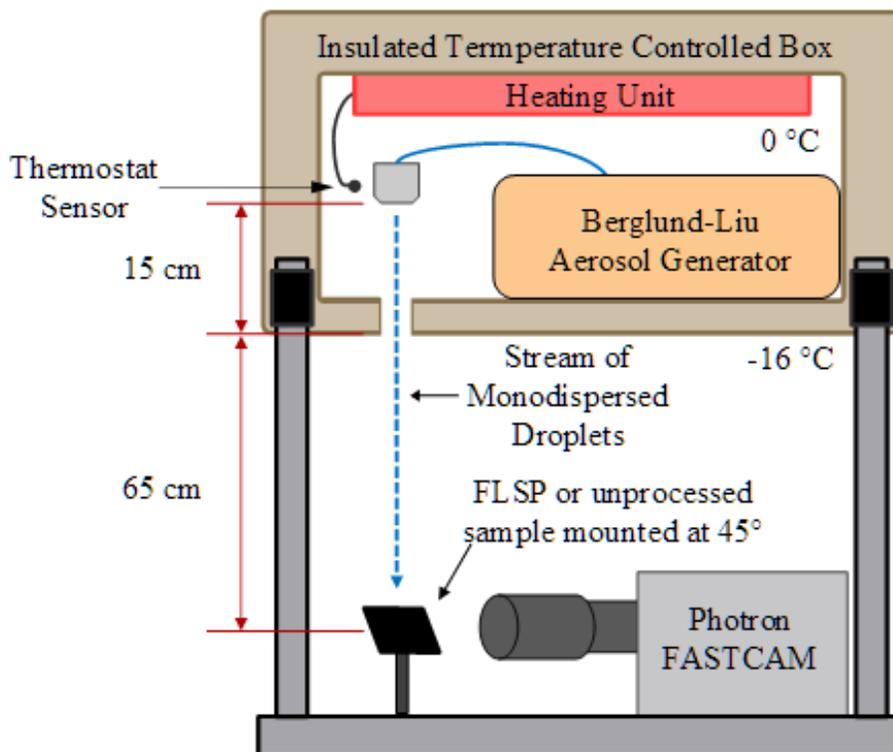
Figure 4.2: Experimental setup for imaging supercooled droplet impact on the unprocessed and FLSP surface.

Only droplets that were in focus for the entirety of their time within the field of view prior to impact, were used as the droplets of interest for this study. Still frame images of a typical droplet falling and impacting the surface is shown in Figure 4.3. As the droplet fully enters the field of view (Figure 4.3a), pixel locations of the droplet boundaries (top, bottom, left, right) were measured in two frame increments until the frame in which impact occurs (Figure 4.3g). These boundaries were used to determine the average diameter, both perpendicular to flow (D_x) and parallel to flow (D_y), for each droplet. The droplet position upon fully entering the field of view and at impact was used for determining the droplet velocity at impact (V_{impact}). D_x, D_y and V_{impact} were important parameters for estimating the temperature at impact for each droplet.

150 μm

| (a) | (b) | (c) | (d) | (e) | (f) | (g) | (h) | (i) | (j) |
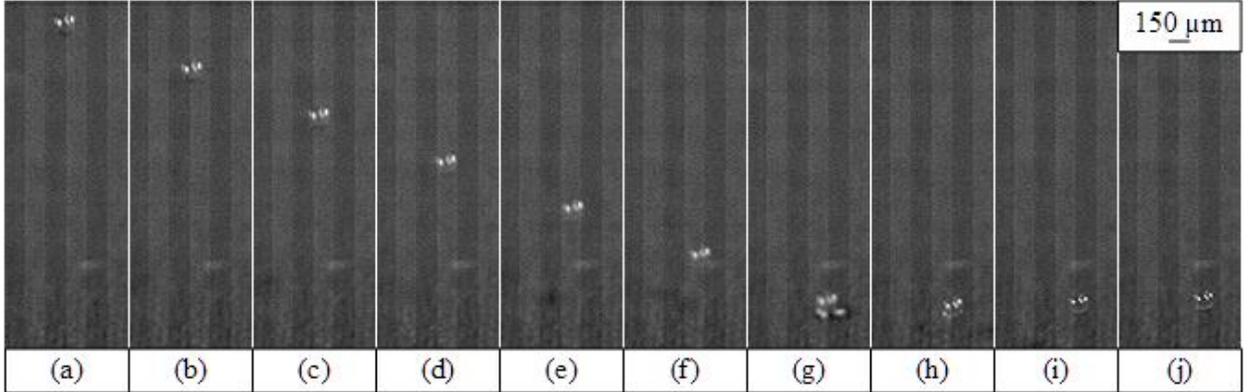
Figure 4.3: Droplet entering field of view (a), falling to surface (b-f), impacting surface (g), and bouncing away from the surface (h-j). The droplet position is shown in 10 frame increments. Time: -4 ms (a), -3.33 ms (b), -2.67 ms (c), -2 ms (d), -1.33 ms (e), -0.67 ms (f), impact (g), 0.67 ms (h), 1.33 ms (i), 2 ms (j).

4.3 Theoretical Terminal Velocity of Droplet

Droplets impacting the surface were assumed to have reached terminal velocity. At terminal velocity the gravitational force on the droplet (F_g), the buoyant force on the droplet (F_b), and the drag force (F_d) on the droplet sum to zero:

$$F_g - F_b = F_d \qquad (1)$$

$$\frac{\pi D_{eq}^3 (\rho_w - \rho_a)g}{6} = \frac{\rho_a V_t^2 C_D \pi D_{eq}^2}{8} \qquad (2)$$

Thus, the terminal velocity (V_t) of a spherical falling droplet is a function of: the density of the water (ρ_w), the density of the air (ρ_a), the volume equivalent diameter of the spheroid droplets (D_{eq}), the gravitational constant (g), and the drag coefficient (C_D):

$$V_t = \sqrt{\frac{4(\rho_w - \rho_a)D_{eq}g}{3\rho_a C_D}} \qquad (3)$$

For the case of a spherical droplet falling through still air, the Reynolds number (Re) is a function of the velocity of the droplet (V), the diameter of the droplet (D_{eq}), and the kinematic viscosity of the air (ν_a):

$$Re = \frac{V\,D_{eq}}{\nu_a} \qquad (4)$$

The relationship between the drag coefficient for uniform flow around a sphere has been derived by Morrison [50]. This relationship is valid for the range of Reynolds numbers included in this study. Thus for the case of a falling spherical droplet, the drag coefficient (C_D) is a function of the Reynolds number (Re):

$$C_d = \frac{24}{Re} + \frac{2.6\left(\frac{Re}{5.0}\right)}{1+\left(\frac{Re}{5.0}\right)^{1.52}} + \frac{0.411\left(\frac{Re}{2.63x10^5}\right)^{-7.94}}{1+\left(\frac{Re}{2.63x10^5}\right)^{-8.00}} + \frac{0.25\left(\frac{Re}{10^6}\right)}{1+\left(\frac{Re}{10^6}\right)} \qquad (5)$$

The Reynolds number at impact can be calculated by substituting the experimentally measured droplet velocity and spheroidal equivalent diameter into Equation 4. The drag coefficient at impact can then be calculated by substituting the Reynolds number at impact into Equation 5. The theoretical terminal velocity can be calculated through iteration of Equations 5, 3, and 4. Iteration should be continued until the value of Equation 3 converges. Iteration steps are shown in Figure 4.4.

V_{impact}

V_n

$$Re = \frac{V_n D_{eq}}{\nu_a} \quad (4)$$

$$C_d = \frac{24}{Re} + \frac{2.6\left(\frac{Re}{5.0}\right)}{1 + \left(\frac{Re}{5.0}\right)^{1.52}} + \frac{0.411\left(\frac{Re}{2.63x10^5}\right)^{-7.94}}{1 + \left(\frac{Re}{2.63x10^5}\right)^{-8.00}} + \frac{0.25\left(\frac{Re}{10^6}\right)}{1 + \left(\frac{Re}{10^6}\right)} \quad (5)$$

$V_t = V_{n+1}$

$$V_t = \sqrt{\frac{4(\rho_w - \rho_a)D_{eq}g}{3\rho_a C_D}} \quad (3)$$

Convergence — no

yes

$V_t = V_{n+1}$
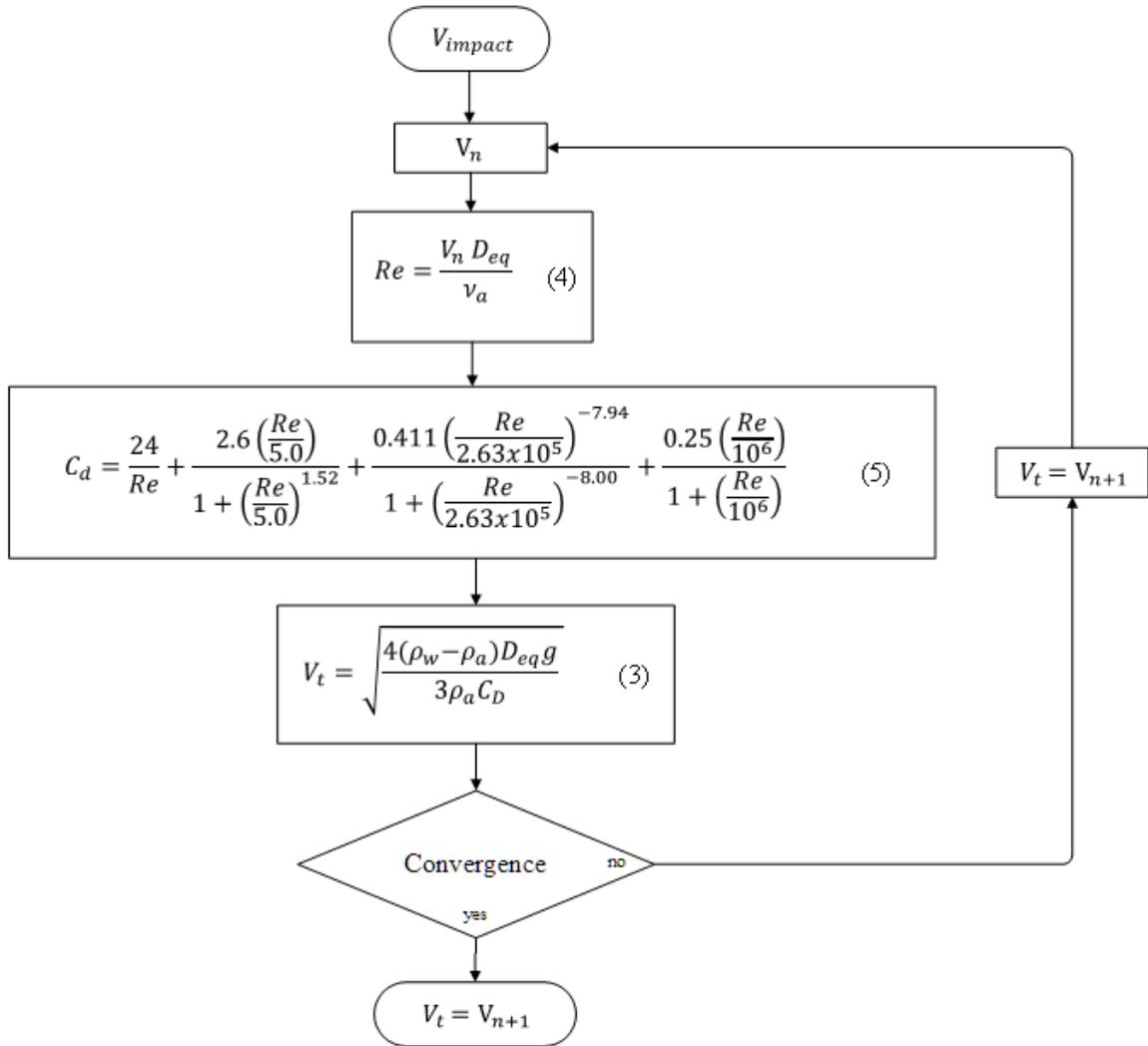
Figure 4.4: Iterative process for determining terminal velocity.

For a droplet not at terminal velocity, the drag force must be considered as a force which impacts the acceleration of the droplet. The drag force of a spherical particle in a flow is function of the drag coefficient (C_d), density of the air (ρ_a), velocity of the droplet (V), and the projected area of the droplet (A_p):

$$F_d = \frac{1}{2}C_d\rho_a V^2 A_p \quad (6)$$

The instantaneous acceleration of a droplet can be calculated by dividing the sum of the forces at that time by the mass of the droplet. An estimation of the change in velocity for a unit time can be calculated by multiplying the instantaneous acceleration by the unit of time.

4.4 Droplet Cooling

As the droplet falls, the temperature of the droplet will approach the temperature of the surrounding environment. In the case of free falling liquid drops, the Ranz-Marshall correlation can be used to determine the mean Nusselt number, a dimensionless heat transfer coefficient [51]. The Ranz-Marhall correlation states that the mean Nusselt number ($\overline{Nu_D}$) of the droplet is a function of the Reynolds number (Re) and the Prandtl number of the air (Pr):

$$\overline{Nu_D} = 2 + 0.6Re^{1/2}Pr^{1/3} \tag{7}$$

The mean convective heat transfer coefficient ($\bar{h}$) is a function of the mean Nusselt number ($\overline{Nu_D}$), the thermal conductivity of the air (k_a), and the diameter of the droplet (D):

$$\bar{h} = \frac{\overline{Nu_D}k_a}{D} \tag{8}$$

The Biot number is a ratio used to determine whether convection or conduction is the rate controlling process of heat transfer. For a spherical particle, the Biot number is a function of the mean heat transfer coefficient ($\bar{h}$), the droplet diameter (D), and the thermal conductivity of the water (λ_w):

$$Bi = \frac{\bar{h}D}{2\lambda_w} \tag{9}$$

For $Bi < 0.1$, the temperature gradient inside the droplet is negligible. Thus, the lumped capacitance model can be applied. The lumped capacitance model assumes a spatially uniform temperature distribution that is only dependent on time. For the case of a droplet in free fall, the temperature of the droplet (T) is a function of the temperature of the air (T_∞), the initial temperature of the droplet (T_0), time (t), and the thermal time constant (τ):

$$\frac{T - T_\infty}{T_0 - T_\infty} = e^{-\frac{t}{\tau}} \tag{10}$$

For the case of a free falling droplet, the thermal time constant (τ) is a function of the diameter of the droplet (D), the density of the water (ρ_w), the heat capacity of the water ($C_{p,w}$), and the mean convective heat transfer coefficient ($\bar{h}$):

$$\tau = \frac{D\rho_w C_{p,w}}{6\bar{h}} \tag{11}$$

It is important to note that with regards to the equations shown, the density [52], kinematic viscosity [53], heat capacity [54], and thermal conductivity [55] of supercooled water vary significantly from their respective values at STP. The density, kinematic viscosity, thermal conductivity and Prandtl number of air at subzero temperatures also vary from their respective values at STP [56]. These properties are shown for the experimental conditions in Table 4.1.

Table 4.1: Properties of water and air for experimental conditions.

Temperature		Water				Air			
		Density	Kinematic Viscosity	Heat Capacity	Thermal Conductivity	Density	Kinematic viscosity	Thermal Conductivity	Prandtl Number
T		ρ_w	ν_w	$C_{p,w}$	λ_w	ρ_a	ν_a	k_a	Pr
		[52]	[53]	[54]	[55]	[56]	[56]	[56]	[56]
K	°C	kg/m^3	m^2/s	J/kg.K	W/m.K	kg/m^3	m^2/s	W/m.K	-
273.15	0	999.832	1.79E-06	4216.46	0.556	1.292	1.33E-05	2.420E-02	0.71204
272.15	-1	999.758	1.86E-06	4222.73	0.553	1.297	1.32E-05	2.412E-02	0.71221
271.15	-2	999.664	1.93E-06	4225.52	0.550	1.302	1.31E-05	2.404E-02	0.71238
270.15	-3	999.550	2.01E-06	4232.37	0.548	1.307	1.30E-05	2.397E-02	0.71255
269.15	-4	999.414	2.01E-06	4237.45	0.545	1.311	1.29E-05	2.389E-02	0.71271
268.15	-5	999.256	2.16E-06	4243.50	0.542	1.316	1.28E-05	2.381E-02	0.71288
267.15	-6	999.075	2.25E-06	4250.16	0.539	1.321	1.28E-05	2.374E-02	0.71305
266.15	-7	998.869	2.35E-06	4257.68	0.536	1.326	1.27E-05	2.366E-02	0.71322
265.15	-8	998.638	2.45E-06	4263.79	0.533	1.331	1.26E-05	2.358E-02	0.71338
264.15	-9	998.381	2.55E-06	4275.24	0.530	1.336	1.25E-05	2.351E-02	0.71354
263.15	-10	998.096	2.67E-06	4283.93	0.527	1.341	1.24E-05	2.343E-02	0.71371
262.15	-11	997.783	2.79E-06	4293.75	0.523	1.347	1.23E-05	2.335E-02	0.71387
261.15	-12	997.441	2.91E-06	4307.23	0.520	1.352	1.23E-05	2.327E-02	0.71403
260.15	-13	997.069	3.04E-06	4318.44	0.516	1.357	1.22E-05	2.320E-02	0.71419
259.15	-14	996.665	3.18E-06	4332.01	0.512	1.362	1.21E-05	2.312E-02	0.71435
258.15	-15	996.228	3.35E-06	4347.46	0.509	1.367	1.20E-05	2.304E-02	0.71451
257.15	-16	995.758	3.51E-06	4364.51	0.505	1.373	1.19E-05	2.297E-02	0.71466
256.15	-17	995.252	3.69E-06	4382.25	0.501	1.378	1.18E-05	2.289E-02	0.71482

From the equations shown, the velocity of a droplet can be calculated as a function of time. By comparing the temporal theoretical velocity and the time at which the impact velocity is reached, the droplet temperature can be calculated. The lumped capacitance model is used for calculating the temperature of the droplet at each time.

4.5 Results

The impact dynamics of four droplets, two droplets impacting the unprocessed surface and two droplets impacting the FLSP surface, were studied. The experimentally measured values of D_x, D_y, and V_{impact}, as well as the calculated measurements for the volume equivalent diameter (VED), terminal velocity, and droplet temperature at impact are included in Table 4.2.

The impact velocity of droplet 3 is slightly lower than the calculated terminal velocity. This difference is likely caused by velocity oscillations about the terminal velocity [57]. Due to these oscillations, it is unknown how long droplet 3 was at terminal velocity, thus the corresponding time for heat transfer is not known. For the parameters of droplet 3, terminal velocity is reached at a fall time of approximately 0.1 s, thus the temperature can be expected to have cooled to at least -7 °C. The impact velocity of droplet 1, droplet 2, and droplet 4 are greater than the terminal velocity for those droplets. These differences are due to the fact that the droplets were expelled were expelled from the aerosol with an initial velocity. Given a larger distance to fall, these droplets would reach terminal velocity.

Table 4.2: Experimental and calculated measurements for the four droplets studied.

		Experimental Measurements			Calculated Measurements		
		Dx	Dy	Impact Velocity	VED	Terminal Velocity	Temperature at impact
		[µm]	[µm]	[m/s]	[µm]	[m/s]	°C
Unprocessed Surface CA: 79.2 ± 4.6°	Droplet 1	191.54	241.54	1.24	206.93	0.77	-4.56
	Droplet 2	186.15	248.46	1.33	204.96	0.76	-4.22
FLSP Surface CA: 168.4 ± 1.1°	Droplet 3	160.97	151.94	0.54	157.90	0.56	≤ -7
	Droplet 4	198.57	177.86	1.22	191.41	0.70	-4.61

The calculated velocity of the four droplets as a function of time is shown in Figure 4.5. The temperature of each droplet at impact can be correlated to the time at which the impact velocity is reached. Droplet temperature as a function of time after being ejected is shown in Figure 4.6.
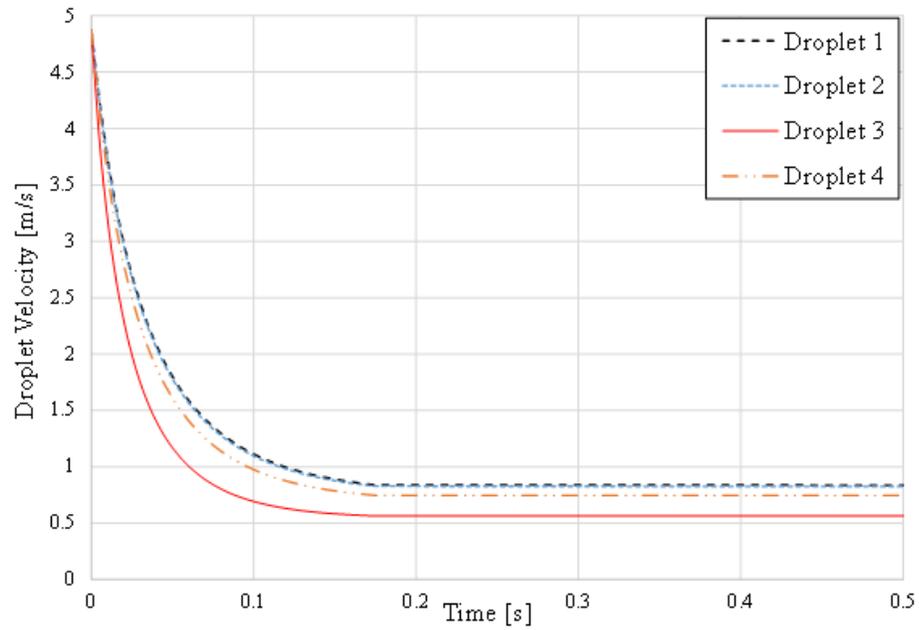
Figure 4.5: Calculated velocity as a function of time for the droplets. Droplet is expelled from aerosol generator at 0 seconds.
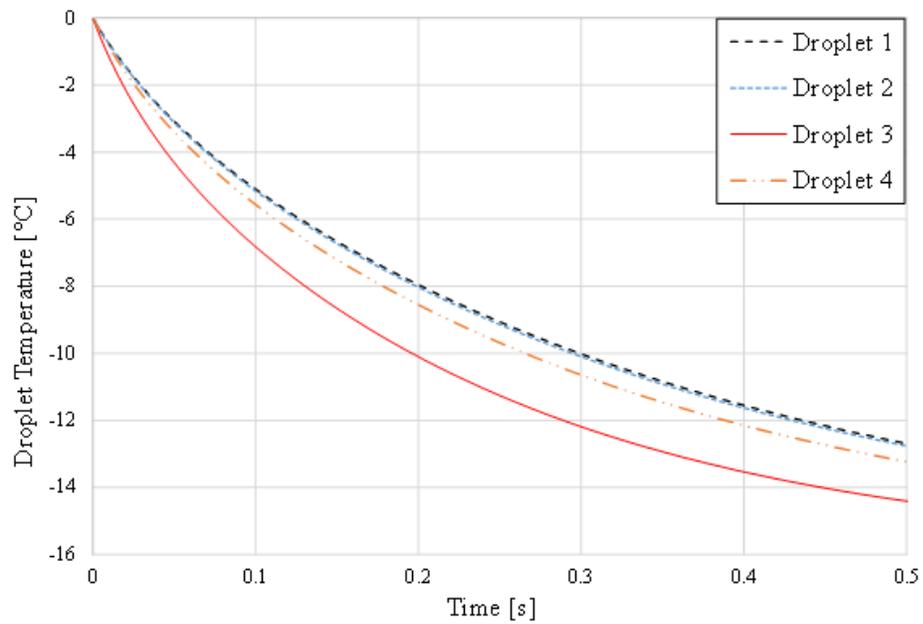
Figure 4.6. Droplet temperature as a function of time. Droplet is expelled from aerosol generator at 0 seconds.

4.6 Supercooled droplet impact onto unprocessed surface

Still frame images of droplet 1 and droplet 2 impacting the unprocessed sample are shown in Figure 4.8 and Figure 4.9 respectively. After impact, neither droplet can overcome the adhesive force with the surface and, thus, both freeze to the unprocessed surface. One can hypothesize that in the time required for the droplet motion to stop: ice nucleation was initiated (likely at the instant impact occurs [12, 37]), then propagated through the entire volume of droplet. Because the velocity of the dendritic freezing front is dependent on the level of supercooling of the droplet [13, 58], the time required for droplet motion to cease after impact can serve as a verification of the droplet temperature at impact. It is not expected that the second phase of supercooled freezing will be observed during our study. The necessary distances for dendritic front velocity is shown in Figure 4.7.
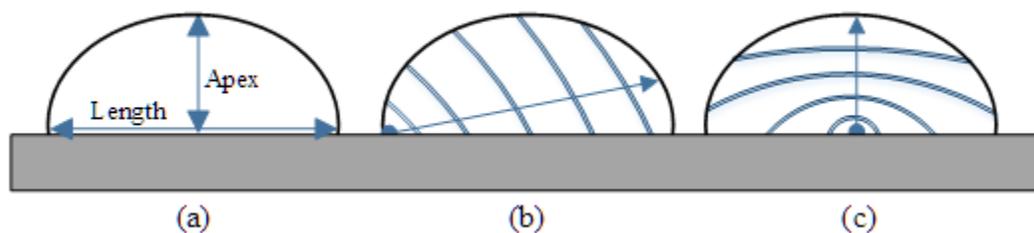
Figure 4.7: (a) Definition defining apex and length of sessile droplet. (b) Dendritic propagation direction from nucleation site at the TCL. (c) Dendritic propagation direction from point of impact at SL.

Nucleation during supercooled freezing is expected to initiate at the site of lowest energy. Previous literature has shown nucleation occurs at the solid-liquid (SL) interface or along the triple phase contact line (TCL). The exact location of the nucleation site, however, is not a well understood phenomenon, and cannot be examined using the current experimental setup. An approximate location of the nucleation site in this study can be estimated using the time for droplet motion to stop after impact and the dimensions of the droplet at that time. Through frame by frame analysis of droplet 1 it was determined that a cessation of motion took 6.6 ms (99 frames) while droplet 2 stopped in 7.87 ms (118 frames). The apex and length of droplet 1 are 90 µm and 230

µm, respectively, while the apex and length of droplet 2 are 120 µm and 200 µm, respectively. For nucleation originating at the SL interface, the freezing front would need to propagate to the apex of the droplet. If originating from the TCL, the freezing front would need to propagate the diameter of the TCL for the droplet. In the case of droplet 1, for freezing to occur in 6.6 ms with a nucleation site originating at the SL interface, the front velocity would be 0.0136 m/s, indicating a droplet temperature of approximately -7 °C. If nucleation originated from the TCL the front velocity would be 0.0348 m/s, indicating a droplet temperature of approximately -10 °C. Given that the temperature of droplet 1 was calculated to be -4.56 °C, it is more likely that the nucleation initiated near the impact location along the SL rather than the TCL. In the case of droplet 2, for freezing to occur in 7.87 ms with a nucleation site originating at the SL, the front velocity would be 0.01524 m/s, indicating a droplet temperature of approximately -7.5 °C. If nucleation originated from the TCL, the front velocity would be 0.0254 m/s, indicating a droplet temperature of approximately -10 °C. Given that the temperature of droplet 2 was calculated to be -4.22 °C, it is more likely that the nucleation initiated near the impact location along the SL rather than the TCL. The relationship between dendrite front velocity and droplet temperature is shown by data shown by Schremb et al. [13].
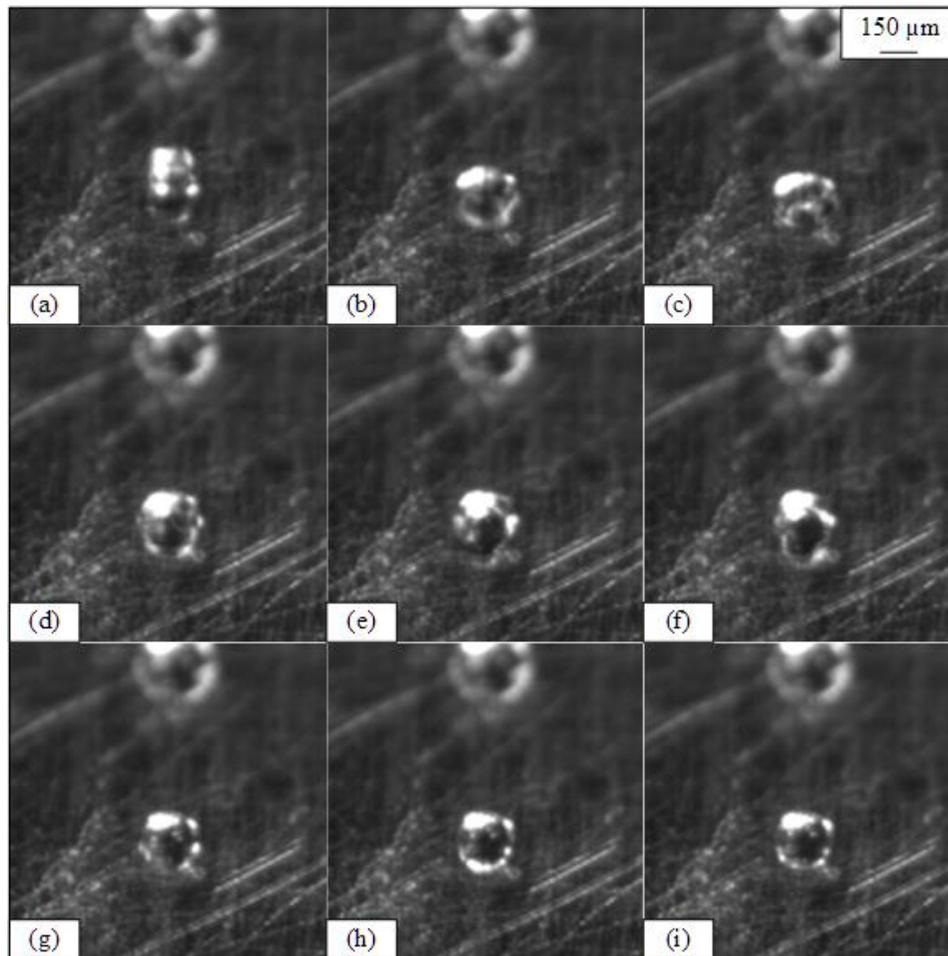
Figure 4.8: Still frame images during the impact of Droplet 1. Time: 0 ms (a), 0.067 ms (b), 0.133 ms (c), 0.2 ms (d), 0.267 ms (e), 0.33 ms (f), 1 ms (g), 1.67 ms (h), 2.33 ms (i).
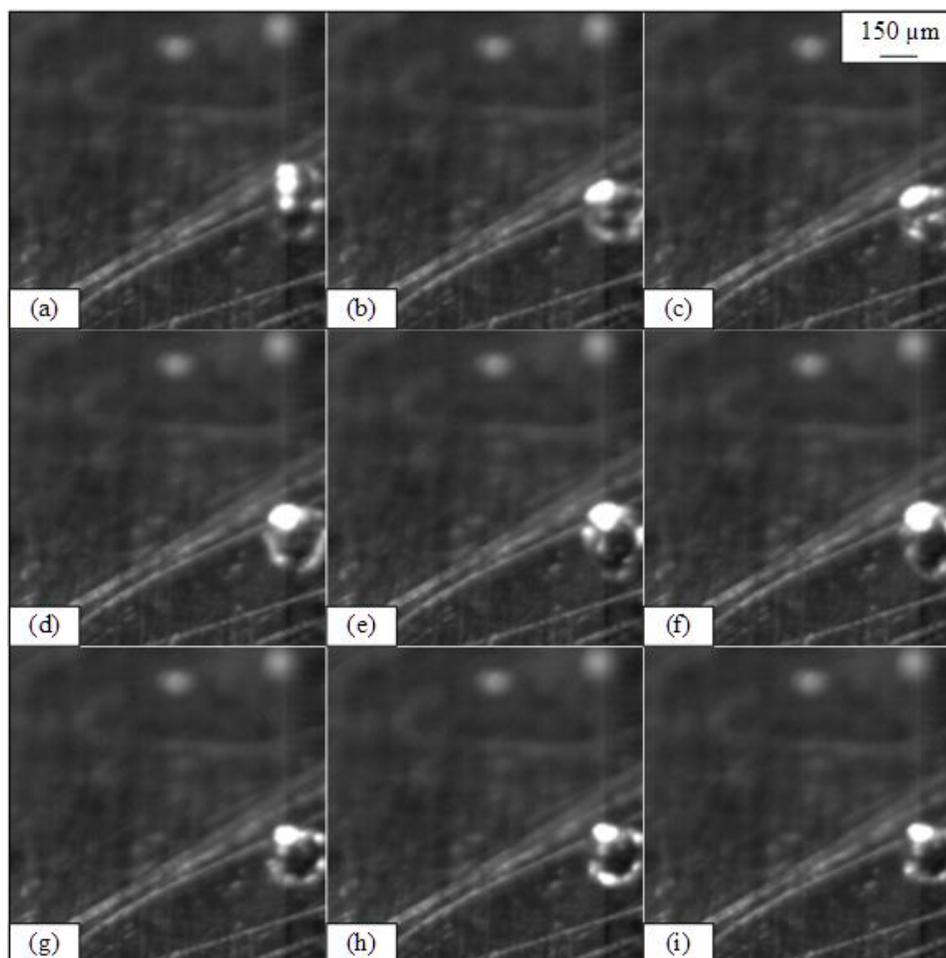
Figure 4.9: Still frame images during the impact of Droplet 2. Time: 0 ms (a), 0.067 ms (b), 0.133 ms (c), 0.2 ms (d), 0.267 ms (e), 0.33 ms (f), 1 ms (g), 1.67 ms (h), 2.33 ms (i).

4.7   Supercooled Droplet Impact onto FLSP Surface

Still frame images of droplet 3 and droplet 4 impacting the superhydrophobic FLSP sample are shown in Figure 4.10 and Figure 4.11 respectively. Both droplets bounced off the surface shortly after initial impact. Droplet 3 was in contact with the surface for 0.267 ms while droplet 4 was in contact with the surface for 0.333 ms. For droplets 3 and 4, ice nucleation is not likely to be initiated by the lowering of the droplet temperature during contact. Any conductive heat transfer between the superhydrophobic surface and the droplet is limited by the short time frame of impact and the limited spatial interaction because of the high contact angle with the surface. For nucleation to occur, the nucleation must by initiated by the impact dynamics of the droplet on the surface. For both droplet 3 and droplet 4, it is unknown if nucleation was triggered at impact.

However, if the impact dynamics were to trigger nucleation, it is hypothesized that the rapid evaporative processes of supercooled freezing could aid in the removal of the droplets from the surface as shown by Schutzius et al [59].
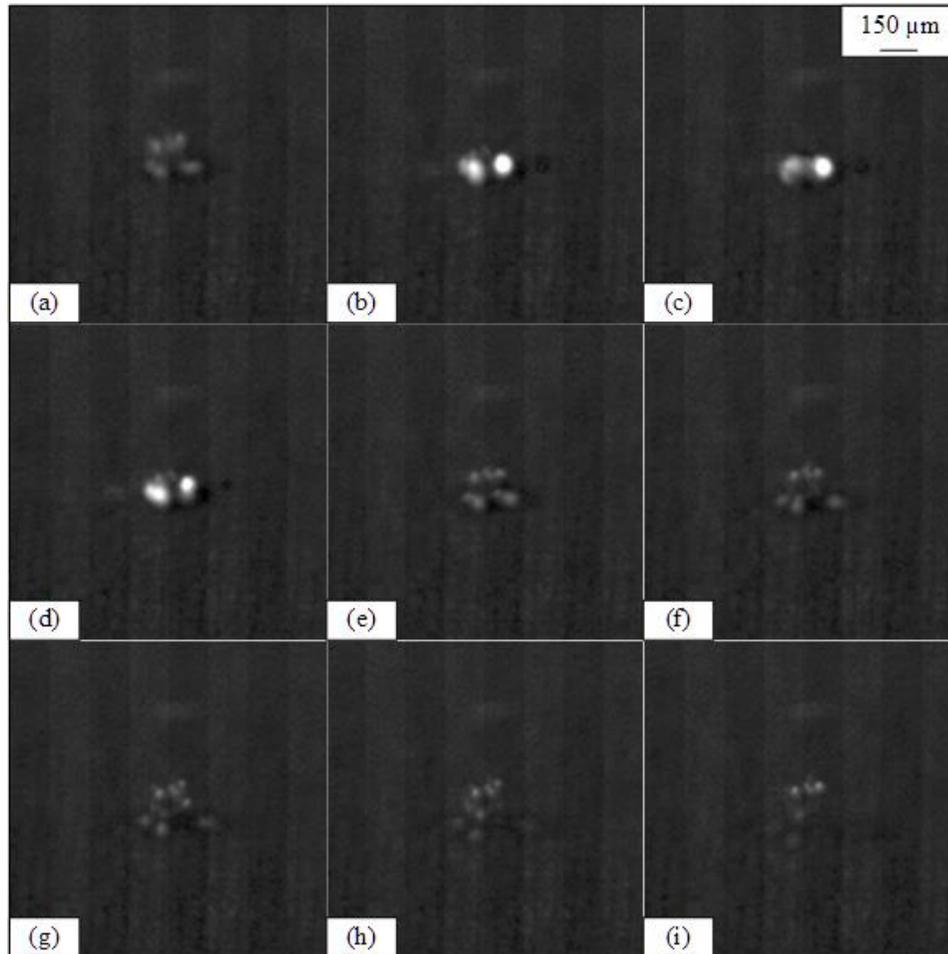
Figure 4.10: Still frame images during the impact of droplet 3.Time: -5 ms (a), 0 ms (b), 1 ms (c), 2 ms (d), 0.267 ms (e), 0.333 ms (f), 0.400 ms (g), 0.467ms (h), 0.533ms (i).
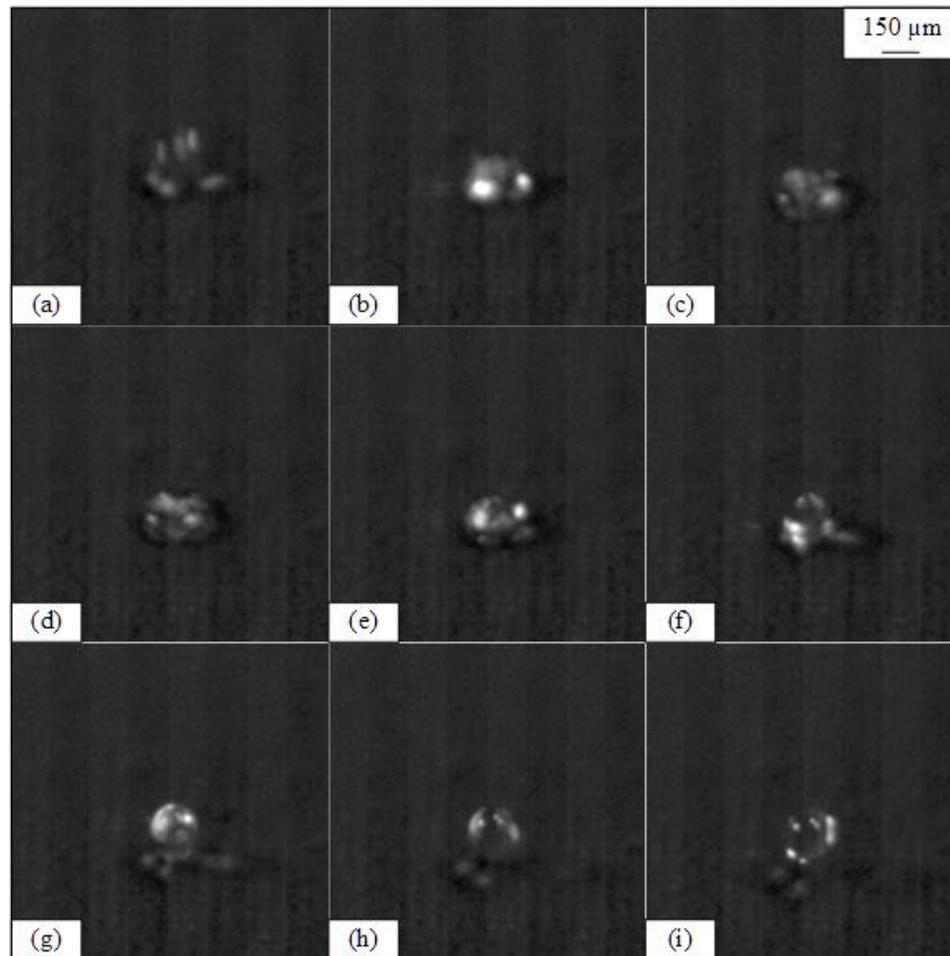
Figure 4.11: Still frame images during the impact of Droplet 4. Time: 0 ms (a), 0.067 ms (b), 0.133 ms (c), 0.200 ms (d), 0.267 ms (e), 0.333 ms (f), 0.400 ms (g), 0.467ms (h), 0.533ms (i).

4.8 Conclusion

In this work, imaging of supercooled water droplet interaction dynamics on a solid aluminum 7075-O Clad cold substrate for a droplet diameter below 160 µm is shown for the first time. Results indicate that microscale supercooled water droplets at low velocities will stick and freeze to unprocessed aluminum 7075-O Clad surfaces, while FLSP surfaces will repel droplets under similar conditions. A method for estimating the cooling of small falling water droplets in an environment of about -16 °C is described. This method gives insights for determining the temperature of supercooled droplets for the range of droplet diameters used in the experimental studies included in

this work. In addition, a way to estimate the nucleation site of a supercooled droplet by extrapolation of dendrite front velocity is provided.

References

[1]   F. Feuillebois, a. Lasek, P. Creismeas, F. Pigeonneau, and a. Szaniawski, "Freezing of a Subcooled Liquid Droplet," *Journal of Colloid and Interface Science*, vol. 169, no. 1. pp. 90–102, 1995.

[2]   K. Fumoto and T. Kawanami, "Study on Freezing Characteristics of Supercooled Water Droplets Impacting on Solid Surfaces," *J. Adhes. Sci. Technol.*, vol. 26, no. 26, pp. 4–5, 2012.

[3]   I. N. S. Based and I. W. Droplets, "Design of Ice-free Nanostructured Impacting Water Droplets," *ACS Appl. Mater. Interfaces*, vol. 4, no. 12, pp. 7699–7707, 2010.

[4]   E. B. Moore and V. Molinero, "Structural transformation in supercooled water controls the crystallization rate of ice," *Nature*, vol. 479, no. 7374, pp. 506–508, 2011.

[5]   M.-H. Kim, D. R. Kim, and K.-S. Lee, "Stochastic approach to the anti-freezing behaviors of superhydrophobic surfaces," *Int. J. Heat Mass Transf.*, vol. 106, pp. 841–846, 2017.

[6]   A. Criscione, I. V Roisman, S. Jakirli, and C. Tropea, "Towards modelling of initial and final stages of supercooled water solidification," *Int. J. Therm. Sci.*, vol. 92, pp. 150–161, 2015.

[7]   J. B. Boreyko, R. R. Hansen, K. R. Murphy, S. Nath, S. T. Retterer, and C. P. Collier, "Controlling condensation and frost growth with chemical micropatterns," *Sci. Rep.*, no. 6, pp. 1–15, 2016.

[8]   P. G. Debenedetti, "Supercooled and glassy water," *J. Phys. Condens. Matter*, vol. 15, no. 45, 2003.

[9] D. Turnbull, "Kinetics of Heterogeneous Nucleation," *J. Chem. Phys.*, vol. 18, no. 2, pp. 198–203, 1950.

[10] C. Goy, M. A. C. Potenza, S. Dedera, M. Tomut, E. Guillerm, A. Kalinin, K.-O. Voss, A. Schottelius, N. Petridis, A. Prosvetov, G. Tejeda, J. M. Fernández, C. Trautmann, F. Caupin, U. Glasmacher, and R. E. Grisenti, "Shrinking of Rapidly Evaporating Water Microdroplets Reveals their Extreme Supercooling," *Phys. Rev. Lett.*, pp. 1–14, 2017.

[11] S. Jung, M. K. Tiwari, N. V. Doan, and D. Poulikakos, "Mechanism of supercooled droplet freezing on surfaces.," *Nat. Commun.*, vol. 3, p. 615, 2012.

[12] J. Blake, D. Thompson, D. Raps, and T. Strobl, "Simulating the Freezing of Supercooled Water Droplets Impacting a Cooled Substrate," *AIAA J.*, vol. 53, no. 7, pp. 1725–1739, 2015.

[13] M. Schremb and C. Tropea, "Solidification of supercooled water in the vicinity of a solid wall," *Phys. Rev. E*, vol. 94, no. 5, p. 52804, Nov. 2016.

[14] A. G. Marinn, O. R. Enriquez, P. Brunet, P. Colinet, and J. H. Snoeijer, "Universality of tip singularity formation in freezing water drops," *Phys. Rev. Lett.*, vol. 113, no. 5, pp. 1–5, 2014.

[15] M. Nauenberg, "Theory and experiments on the ice-water front propagation in droplets freezing on a subzero surface," *Eur. J. Phys.*, vol. 37, no. 4, 2016.

[16] M. Nauenberg, "Conical tip in frozen water drops," *arXiv*, vol. 95064, p. 6, 2014.

[17] W. Kong and H. Liu, "A theory on the icing evolution of supercooled water near solid substrate," *Int. J. Heat Mass Transf.*, vol. 91, pp. 1217–1236, 2015.

[18] S. Jung, M. K. Tiwari, and D. Poulikakos, "Frost halos from supercooled water droplets.," *Proc. Natl. Acad. Sci. U. S. A.*, vol. 109, no. 40, pp. 16073–8, 2012.

[19] L. Oberli, D. Caruso, C. Hall, M. Fabretto, P. J. Murphy, and D. Evans, "Condensation and freezing of droplets on superhydrophobic surfaces," *Adv. Colloid Interface Sci.*, vol. 210, pp. 47–57, 2014.

[20] C. A. Zuhlke, T. P. Anderson, and D. R. Alexander, "Comparison of the structural and chemical composition of two unique micro/nanostructures produced by femtosecond laser interactions on nickel," *Appl. Phys. Lett.*, vol. 103, no. 12, 2013.

[21] J. M. Liu, "Simple technique for measurements of pulsed Gaussian-beam spot sizes," *Opt. Lett.*, vol. 7, no. 5, p. 196, 1982.

[22] C. A. Zuhlke, T. P. Anderson, and D. R. Alexander, "Formation of multiscale surface structures on nickel via above surface growth and below surface growth mechanisms using femtosecond laser pulses.," *Opt. Express*, vol. 21, no. 7, pp. 8460–73, Apr. 2013.

[23] M. Lee, C. Yim, and S. Jeon, "Communication: Anti-icing characteristics of superhydrophobic surfaces investigated by quartz crystal microresonators," *J. Chem. Phys.*, vol. 142, no. 4, 2015.

[24] S. Farhadi, M. Farzaneh, and S. A. Kulinich, "Anti-icing performance of superhydrophobic surfaces," *Appl. Surf. Sci.*, vol. 257, no. 14, pp. 6264–6269, 2011.

[25] S. A. Kulinich and M. Farzaneh, "Ice adhesion on super-hydrophobic surfaces," *Appl. Surf. Sci.*, vol. 255, no. 18, pp. 8153–8157, 2009.

[26] L. Makkonen, "Ice Adhesion —Theory, Measurements and Countermeasures," *J. Adhes. Sci. Technol.*, vol. 26, no. 4–5, pp. 413–445, 2012.

[27] S. Jung, M. Dorrestijn, D. Raps, A. Das, C. M. Megaridis, and D. Poulikakos, "Are superhydrophobic surfaces best for icephobicity?," *Langmuir*, vol. 27, no. 6, pp. 3059–3066, 2011.

[28] Q. Hao, Y. Pang, Y. Zhao, J. Zhang, J. Feng, and S. Yao, "Mechanism of delayed frost growth on superhydrophobic surfaces with jumping condensates: More than interdrop freezing," *Langmuir*, vol. 30, no. 51, pp. 15416–15422, 2014.

[29] C. Antonini, M. Innocenti, T. Horn, M. Marengo, and A. Amirfazli, "Understanding the effect of superhydrophobic coatings on energy reduction in anti-icing systems," *Cold Reg. Sci. Technol.*, vol. 67, no. 1–2, pp. 58–67, 2011.

[30] J. B. Boreyko and C. P. Collier, "Delayed frost growth on jumping-drop superhydrophobic surfaces," *ACS Nano*, vol. 7, no. 2, pp. 1618–1627, 2013.

[31] A. S. Van Dyke, D. Collard, M. M. Derby, and A. R. Betz, "Droplet coalescence and freezing on hydrophilic, hydrophobic, and biphilic surfaces," *Appl. Phys. Lett.*, vol. 107, no. 14, pp. 1–5, 2015.

[32] X. Qu, J. B. Boreyko, F. Liu, R. L. Agapov, N. V. Lavrik, S. T. Retterer, J. J. Feng, C. P. Collier, and C. H. Chen, "Self-propelled sweeping removal of dropwise condensate," *Appl. Phys. Lett.*, vol. 106, no. 22, pp. 2–5, 2015.

[33] K. M. Wisdom, J. A. Watson, X. Qu, F. Liu, G. S. Watson, and C.-H. Chen, "Self-cleaning of superhydrophobic surfaces by self-propelled jumping condensate," *Proc. Natl. Acad. Sci.*, vol. 110, no. 20, pp. 7992–7997, 2013.

[34] P. Tourkine, M. Le Merrer, and D. Quéré, "Delayed freezing on water repellent materials," *Langmuir*, vol. 25, no. 13, pp. 7214–7216, 2009.

[35] B. P. Binks and T. S. Horozov, *Colloidal Particles at Liquid Interfaces*. Cambridge University Press, 2006, 2006.

[36] T. Maitra, C. Antonini, M. K. Tiwari, A. Mularczyk, Z. Imeri, P. Schoch, and D. Poulikakos, "Supercooled water drops impacting superhydrophobic textures," *Langmuir*, vol. 30, no. 36, pp. 10855–10861, 2014.

[37] M. Schremb, I. V. Roisman, and C. Tropea, "Transient effects in ice nucleation of a water drop impacting onto a cold substrate," *Phys. Rev. E*, vol. 95, no. 2, p. 22805, 2017.

[38] M. Mohammadi, M. Tembely, and A. Dolatabadi, "Supercooled water droplet impacting superhydrophobic surfaces in the presence of cold air flow," *Appl. Sci.*, vol. 7, no. 2, p. 130, 2017.

[39] M. Mohammadi, M. Tembely, and A. Dolatabadi, "Predictive model of supercooled water droplet pinning/repulsion impacting on a superhydrophobic surface: the role of gas-liquid interface temperature," *Langmuir*, vol. 33, no. 8, p. acs.langmuir.6b04394, 2017.

[40] T. Bobinski, G. Sobieraj, K. Gumowski, J. Rokicki, M. Psarski, J. Marczak, and G. Celichowski, "Droplet impact in icing conditions - The influence of ambient air humidity," *Arch. Mech.*, vol. 66, no. 2, pp. 127–142, 2014.

[41] L. Zheng, Z. Li, S. Bourdo, R. K. Khedir, M. P. Asar, C. C. Ryerson, A. S. Biris, K. R. Khedir, M. P. Asar, C. C. Ryerson, and A. S. Biris, "Exceptional superhydrophobicity and low velocity impact icephobicity of acetone-functionalized carbon nanotube films," *Langmuir*, vol. 27, no. 16, pp. 9936–9943, 2011.

[42] K. R. Khedir, G. K. Kannarpady, H. Ishihara, J. Woo, M. P. Asar, C. Ryerson, and A. S. Biris, "Temperature-dependent bouncing of super-cooled water on teflon-coated superhydrophobic tungsten nanorods," *Appl. Surf. Sci.*, vol. 279, pp. 76–84, 2013.

[43] C. Zhang and H. Liu, "Effect of drop size on the impact thermodynamics for supercooled large droplet in aircraft icing," *Phys. Fluids*, vol. 28, no. 6, 2016.

[44] Y. Liu, L. Moevius, X. Xu, T. Qian, J. M. Yeomans, and Z. Wang, "Pancake bouncing on superhydrophobic surfaces," *Nat. Phys.*, vol. 10, no. June, pp. 515–519, 2014.

[45] P. S. Brown, A. Berson, E. L. Talbot, T. J. Wood, W. C. E. Schofield, C. D. Bain, and J. P. S. Badyal, "Impact of picoliter droplets on superhydrophobic surfaces with ultralow spreading ratios," *Langmuir*, vol. 27, no. 22, pp. 13897–13903, 2011.

[46] D. Hee Kwon and S. Joon Lee, "Impact and wetting behaviors of impinging microdroplets on superhydrophobic textured surfaces," *Appl. Phys. Lett.*, vol. 100, no. 17, pp. 1–5, 2012.

[47] S. G. Cober and G. A. Isaac, "Characterization of aircraft icing environments with Supercooled Large Drops for application to commercial aircraft certification," *J. Appl. Meteorol. Climatol.*, vol. 51, no. 2, pp. 265–284, 2012.

[48] M. Quero, D. W. Hammond, R. Purvis, and F. T. Smith, "Analysis of super-cooled water droplet impact on a thin water layer and ice growth," *44th AIAA Aerosp. Sci. Meet. Exhib.*, no. January, p. 466, 2006.

[49] J. Wu, J. Xia, W. Lei, and B. Wang, "Advanced understanding of stickiness on superhydrophobic surfaces.," *Sci. Rep.*, vol. 3, no. c, p. 3268, 2013.

[50] F. A. Morrison, *Data correlation for drag coefficient for sphere*. New York: Cambridge University Press, 2013.

[51] W. E. Ranz and W. R. Marshall, "Evaporation from drops - Part I and II," *Chemical Engineering Progress*, vol. 48, pp. 141–148, 173–180, 1952.

[52] T. Sotani, J. Arabas, H. Kubota, M. Kijima, and S. Asada, "Volumetric behaviour of water under high pressure at subzero temperature," *High Temp. - High Press.*, vol. 32, no. 4, pp. 433–440, 2000.

[53] J. Hallett, "The Temperature Dependence of the Viscosity of Supercooled Water," *Proc. Phys. Soc.*, vol. 82, no. 6, pp. 1046–1050, 1963.

[54] E. Tombari, C. Ferrari, and G. Salvetti, "Heat capacity anomaly in a large sample of supercooled water," *Chem. Phys. Lett.*, vol. 300, no. 5–6, pp. 749–751, 1999.

[55] M. L. Huber, R. A. Perkins, D. G. Friend, J. V. Sengers, M. J. Assael, I. N. Metaxa, K. Miyagawa, R. Hellmann, and E. Vogel, "New International Formulation for the Thermal Conductivity of H2O," *J. Phys. Chem. Ref. Data*, vol. 41, no. 3, pp. 0–23, 2012.

[56] J. C. Dixon, "Appendix B Properties of Air," in *The Shock Absorber Handbook*, 2nd ed., London: John Wiley & Sons Ltd, 1992, pp. 375–378.

[57] S. Von Kann, J. H. Snoeijer, and D. Van Der Meer, "Velocity oscillations and stop-go cycles: The trajectory of an object settling in a cornstarch suspension," *Phys. Rev. E - Stat. Nonlinear, Soft Matter Phys.*, vol. 87, no. 4, pp. 1–14, 2013.

[58] A. A. Shibkov, Y. I. Golovin, M. A. Zheltov, A. A. Korolev, and A. A. Leonov, "Morphology diagram of nonequilibrium patterns of ice crystals growing in supercooled water," *Phys. A Stat. Mech. its Appl.*, vol. 319, pp. 65–79, 2003.

[59] T. M. Schutzius, S. Jung, T. Maitra, G. Graeber, M. Köhme, and D. Poulikakos, "Spontaneous droplet trampolining on rigid superhydrophobic surfaces," *Nature*, vol. 527, no. 7576, pp. 82–85, 2015.

Appendix

A.1 FLSP structures on Al 7075-O Clad
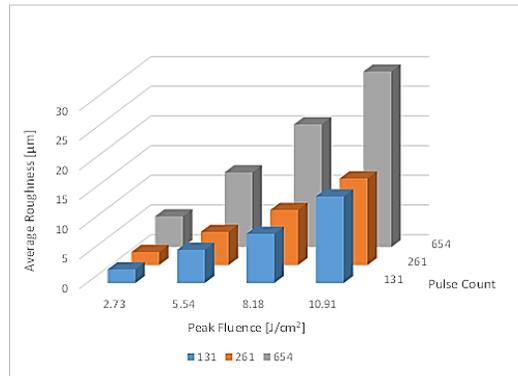
Figure A.1: Average roughness values of FLSP Al 7075-O Clad for 12 combinations of laser fluence and pulse count.
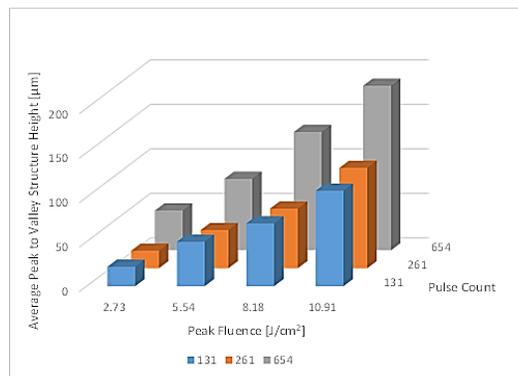
Figure A.2: Average structure peak to valley height of FLSP Al 7075-O Clad for 12 combinations of laser fluence and pulse count.
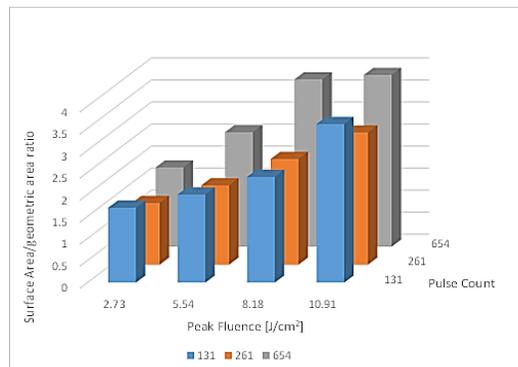
Figure A.3: Surface area to area ratio of FLSP Al 7075-O Clad 12 combinations of laser fluence and pulse count.